sustainability

MDPI

Article

Ultrasound-Induced Embedded-Silica Migration to Biochar Surface: Applications in Agriculture and Environmental Sustainability

Muhammad Abdullah, Shanza Baig, Maria Paula Hernández Martinez and Baharak Sajjadi *

Mewbourne School of Petroleum and Geological Engineering, University of Oklahoma, Norman, OK 73019, USA
* Correspondence: baharak.sajjadi@ou.edu; Tel.: +1-405-325-2921

Abstract

Silicon (Si)–containing compounds, such as silica (SiO_2), play a crucial role as fillers, binding phases, and linking agents in sustainable materials. Coating biochar with SiO_2 can enhance its performance as a carbon-negative filler in composites such as bioplastics, rubber, asphalt, and cement, making it more competitive with conventional fillers. Biochar, derived from biomass pyrolysis, contains a high concentration of biogenic SiO_2—typically 50–80% of its total inorganic content. However, conventional extraction methods such as solvent extraction or gasification detach SiO_2 from the biochar matrix, leading to energy-intensive and environmentally unfavorable processes. The objective of this study was to develop an environmentally friendly and energy-efficient approach to induce the migration of embedded biogenic SiO_2 from within biochar to its surface—without detachment—using ultrasonic treatment. Fifteen biochar samples were produced by pyrolyzing five biomass types (sugarcane bagasse, miscanthus, wheat straw, corn stover, and railroad ties) at 650, 750, and 850 °C. Each sample was subsequently subjected to ultrasonic irradiation in an isopropanol–water mixture for 1 and 2 min. Scanning Electron Microscopy (SEM) and Energy-Dispersive X-ray Spectroscopy (EDS) analyses confirmed that ultrasound treatment significantly enhanced SiO_2 migration to the biochar surface, with up to a 2.5-fold increase in surface Si and O concentrations after 2 min of sonication. The effect was most pronounced for biochar synthesized at 850 °C, corresponding to higher surface porosity and structural stability. Fourier Transform Infrared (FTIR) spectroscopy revealed an increased intensity of the Si–O–Si asymmetric stretching band at 1030 cm^{-1}, indicating surface enrichment of siloxane networks and rearrangement of Si-containing functional groups. Overall, the results demonstrate that ultrasound-assisted treatment is a viable and sustainable technique for enhancing SiO_2 surface concentration and modifying the surface chemistry of biochar. This SiO_2-enriched biochar shows potential for advanced applications in soil amendment, CO_2 capture, water purification, and as a reactive additive in cementitious and asphalt composites.

Keywords: pyrolysis; biochar; ultrasound waves; surface engineering; silica; filler

check for updates

Academic Editors: Rosa Rodriguez, Germán Mazza and María Paula Fabani

Received: 19 October 2025
Revised: 9 November 2025
Accepted: 13 November 2025
Published: 2 December 2025

Citation: Abdullah, M.; Baig, S.; Martinez, M.P.H.; Sajjadi, B. Ultrasound-Induced Embedded-Silica Migration to Biochar Surface: Applications in Agriculture and Environmental Sustainability. *Sustainability* **2025**, *17*, 10813. https://doi.org/10.3390/su172310813

Copyright: © 2025 by the authors. Licensee MDPI, Basel, Switzerland. This article is an open access article distributed under the terms and conditions of the Creative Commons Attribution (CC BY) license (https://creativecommons.org/licenses/by/4.0/).

1. Introduction

The Food and Agriculture Organization of the United Nations (FAO) data for 2022 reveals significant crop residue (biomass) burning practices both globally and in the United States. On a global scale, maize (corn) residue burning was the most substantial at 203.47 million tonnes of dry matter, followed by rice at 90.77 million tonnes, wheat

Downloaded from SHAREOK. Persistent Handle URL: https://hdl.handle.net/11244/343000

at 87.66 million tonnes, and sugarcane at 16.96 million tonnes. In the United States, maize residue burning led with 32.05 million tonnes (15.75% of global), followed by wheat at 5.74 million tonnes (6.55% of global), rice at 0.48 million tonnes (0.53% of global), and sugarcane at 0.24 million tonnes (1.44% of global). Crop residue (biomass) burning poses significant environmental and health risks, contributing to air pollution, climate change, and soil degradation while releasing harmful particulate matter and greenhouse gases into the atmosphere [1,2]. Biomass burning poses risks to both the environment and human health while also leading to the loss of valuable elements and compounds present in biomass [3–8], which should be preserved. Instead of burning, biomass can be utilized through more sustainable processes like pyrolysis, which produce valuable products, including syngas, bio-oil, and biochar [9].

Biochar is a carbon-rich material produced from the pyrolysis of biomass under limited oxygen conditions. It is widely used for soil improvement, carbon sequestration, pollutant adsorption, and as a filler in composites due to its porous structure and stability. Silica (SiO_2) is a common inorganic component in biochar, especially when derived from plant-based biomass like rice husks, wheat straw, and other silica-rich feedstocks. The origin of silica in biochar comes primarily from the biomass feedstock used in its production. Silicon (Si) is widely found in biomass (0.1–10%) and is considered an essential nutrient for the growth of rice husk (18% [7]), wheat [3], and corn stalk (9.4% [7]) [4–6]. At a low temperature (<250 °C), the polymerizing monosilicic acid in biomass pyrolytic carbon partially forms polymeric silicic acid through carbonization dehydration, resulting in a dense C–Si structure. At a medium temperature (250–350 °C), the morphology of monosilicic acid mainly forms the polymeric silicic acid. Furthermore, at a high charring temperature (500–700 °C), Si crystallizes to form Si crystal minerals. Above this temperature (>700 °C), the embedded Si is converted to SiO_x [10,11]. Hence, Si ash (Si-containing functional groups) is one of the highest inorganic elements in biomass pyrolytic carbon (biochar) [8,12–14], and Si-containing functional groups may present in different forms including $Si(OR)_x$, Si–O–Si, SiO_x, and C–Si [11], with C–Si forming a layered structure of C–Si–C. The current ways to access the embedded biogenic SiO_2 are solvent extraction or gasifying the biochar, processes that release the SiO_2 into the solvent [7] or as fly ash [13–16], respectively. Solvent extraction methods often require strong mineral acids or alkalis which pose environmental hazards and demand extensive reagent use. Gasification or thermal treatments, on the other hand, require prolonged heating at temperatures typically above 600 °C and up to 1000 °C to decompose organic components and release SiO_2 as fly ash or in solution. These processes are energy-intensive and environmentally deleterious, releasing CO, CO_2, and other hazardous gases, while physically detaching SiO_2 from the carbon matrix. Additionally, the associated high temperatures can alter the structural and chemical integrity of biochar, limiting the quality and functional performance of the reclaimed silica. Therefore, while biogenic SiO_2 constitutes a significant proportion (50–80%) of the inorganic content in biochar, accessing it efficiently remains technologically challenging using these conventional methods. These limitations underscore the need for novel, environmentally friendly, and energy-efficient techniques to selectively enrich SiO_2 on biochar surfaces without compromising the biochar matrix.

Considering the very high percentage of Si ash (Si as SiO_2, roughly 50–80% [8,12–14]) in biomass pyrolysis derived biochar, the challenges/in-efficiencies of conventional techniques in accessing embedded biogenic SiO_2 [7,13–16], and the vast applications of SiO_2-coated biochar, the aim of this study is to leverage ultrasound waves to induce the embedded biogenic SiO_2 to migrate to the biochar surface. Additionally, the potential applications for which biochar, with biogenic SiO_2 migrated to its surface (resembling SiO_2-coated biochar), are also briefly discussed.

2. Materials and Methods

In this study, 15 biochar samples, produced by pyrolysis (at three different temperatures: 650 °C, 750 °C and 850 °C) of five distinct biomass types—Sugarcane Bagasse (SG), Miscanthus (MIS), Wheat Straw (WS), Corn Stover (CS), and Railroad Ties (RRTs)—were used. The selected pyrolysis temperatures of 650, 750, and 850 °C were chosen based on their well-documented influence on the physicochemical characteristics and mineral content, particularly silica, in biochar. Literature indicates that pyrolysis within this temperature range effectively enhances biochar stability and increases the concentration and crystallinity of embedded biogenic silica [17]. Temperatures below 600 °C generally do not fully convert silica precursors into stable forms, while temperatures above 900 °C may cause structural alterations that reduce silica accessibility. Thus, the 650–850 °C range optimizes both biochar yield and silica enrichment, promoting desirable surface and pore properties conducive to silica migration and surface modification. The selection of the five biomass feedstocks was based on their diverse chemical compositions and ash silica contents (Tables 1 and 2, respectively), making them representative of common lignocellulosic agricultural residues and energy crops. SB, MIS, WS, and CS are abundant global residues with varying inherent silica levels, while RRTs serve as a contrasting woody biomass source with distinct mineral and organic profiles. This diversity enables a comprehensive investigation of ultrasound-induced silica migration dynamics across biochars with different physical and chemical matrices. Together, these pyrolysis conditions and feedstock selections provide a scientifically robust framework to study the effects of ultrasonic exposure on silica migration from embedded mineral phases to the biochar surface. In a typical experiment, 4 g of biomass was prepared by drying at 60 °C, grinding, and sieving. The sample was then placed in the constant temperature zone of a quartz tube reactor. Prior to pyrolysis, the system was purged with N_2. The furnace was then heated to the desired temperature (650 °C, 750 °C, or 850 °C) at a rate of 20 °C/min, with an N_2 flow rate of 50 mL/min. During pyrolysis, the biomass underwent thermal decomposition in the absence of oxygen, producing biochar, volatile organic compounds (VOCs), and gaseous products. Each biochar sample was then subjected to ultrasound-generated Rayleigh waves in a 50:50 solvent of water and isopropyl alcohol for two different durations: 1 min and 2 min. After ultrasound treatment, scanning electron microscopy (SEM) was employed to determine the presence of SiO_2 on the surface of biochar samples. The concentration of SiO_2 on the surface was compared among three different treatments: one not exposed to ultrasound, one exposed to ultrasound for 1 min, and one exposed to ultrasound for 2 min (as all other variables, such as biomass source and pyrolysis temperature, were kept across the samples). The comparative analysis aimed to assess how varying ultrasound treatment durations induce migration of biogenic SiO_2 from within the biochar structure (through micropores within the biochar structure) to the surface. Ultrasonic treatment was carried out using a VCX-750 ultrasonic processor (Sonics & Materials, Inc., Newtown, CT, USA) operating at a fixed frequency of 20 kHz and 100% amplitude, corresponding to a nominal power of 750 W. Each biochar sample was dispersed in a 50:50 (v/v) isopropanol–water mixture without prior degassing, and the sonication was performed in an open system without active temperature control. Ultrasonic irradiation was applied for 1 min and 2 min under identical conditions. Longer exposure durations were ruled out, as literature reports [18,19] indicate that excessive sonication leads to thermal accumulation and particle re-agglomeration, which reduce surface activation efficiency. Energy-dispersive X-ray spectroscopy (EDS) mapping was also conducted to compare the surface elemental composition and distribution among the three treatments of 15 biochar samples. EDS maps were generated for C, Si, and O, both individually and as a composite map. These surface maps were utilized to visualize the spatial distribution of elements across the biochar surface, revealing the relative concentrations of key elements,

particularly Si and O, which indicate the presence of SiO_2. By examining the surface Si and O maps in conjunction with the C background, we sought to identify areas of increased SiO_2 concentration on the biochar surface. Additionally, Fourier Transform Infrared Spectroscopy (FTIR) was performed to identify the Si-containing functional groups ($Si(OR)_x$, Si–O–Si, SiO_x, and C–Si), which could be present either within the structure or on the surface of the biochar and to assess the impact of ultrasound treatment on these groups. As the objective was to identify the Si-containing functional groups and assess the impact of ultrasound treatment on them, FTIR was performed only on biochar from MIS pyrolyzed at 650 °C, 750 °C, and 850 °C. The analysis compared the FTIR results of biochar produced at the same temperature but subjected to ultrasound for different durations: zero minutes (control), 1 min, and 2 min. This approach allowed us to evaluate how varying ultrasound treatment durations influence the presence and characteristics of Si-containing functional groups, such as $Si(OR)_x$, Si–O–Si, SiO_x, and C–Si. By correlating any observed changes in these functional groups with varying ultrasound treatment durations, we aimed to understand how ultrasound treatment affects the chemical properties of biochar, particularly regarding its Si-containing content.

Table 1. Proximate and ultimate analysis of biomass composition.

Element	Miscanthus (wt%)	Corn Stover (wt%)	Sugarcane Bagasse (wt%)	Wheat Straw (wt%)	Railroad Ties (wt%)
Fixed carbon	13.06	16.7	13.41	13.89	18.9
Volatile	85.53	79.0	76.02	77.04	90.9
Ash	1.40	4.3	10.56	9.07	0.4
Carbon	50.64	48.7	45.24	45.02	61.3
Hydrogen	5.85	5.7	5.38	5.90	6.6
Nitrogen	0.21	0.7	0.36	1.06	0.4
Oxygen	41.88	-	38.41	38.82	28.8
Sulfur	0.01	-	0.05	0.12	0.1

Table 2. Ash composition of biomass samples.

Compound	Miscanthus (wt%)	Corn Stover (wt%)	Sugarcane Bagasse (wt%)	Wheat Straw (wt%)
Al_2O_3	0.29	0.28	7.20	2.77
CaO	18.34	8.99	2.74	10.83
Fe_2O_3	1.20	1.12	2.40	2.99
K_2O	6.44	26.38	4.46	15.45
MgO	9.03	6.09	1.30	2.69
MnO	1.11	0.09	0.06	0.07
Na_2O	0.18	0.08	1.30	1.16
P_2O_5	3.58	2.79	0.95	2.15
SiO_2	52.31	51.99	79.19	58.16
TiO_2	0.02	0.01	0.40	0.11
SO_3	3.15	2.20	0.57	2.34

3. Results and Discussions

3.1. SEM and EDS Analysis

The SEM and EDS analyses of the 15 different biochar samples were summarized in Figures 1–5. The results revealed that ultrasound treatment caused the migration of embedded biogenic SiO_2 to the biochar surface, resulting in a significant concentration of

SiO_2 on the biochar surface. EDS provides elemental analysis [20], enabling identification of specific elements (like Si and O) on the biochar surface. The EDS maps (Figures 1–5) revealed a significant increase in the concentrations of Si and O on the surface of the biochar samples subjected to ultrasound. EDS maps thus further confirmed the presence of SiO_2 on the biochar surface, as Si and O are key components of this compound.

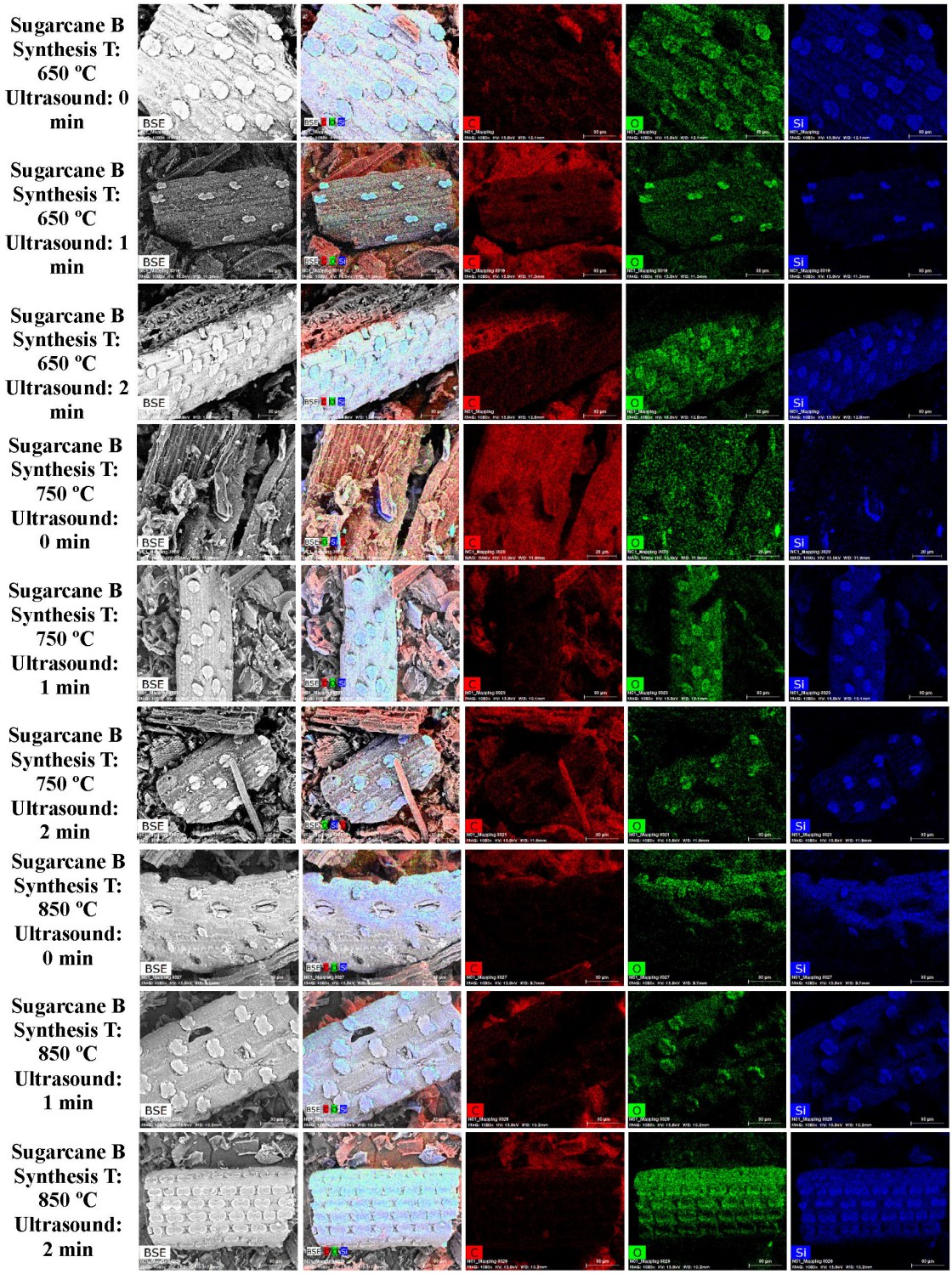


Figure 1. SEM images, BSE images, EDS composite maps, and EDS maps of C, O, and Si elements of biochar samples produced by pyrolysis (at three different temperatures: 650 °C, 750 °C, and 850 °C) of Sugarcane Bagasse and subjected to ultrasound for different durations (1 & 2 min).

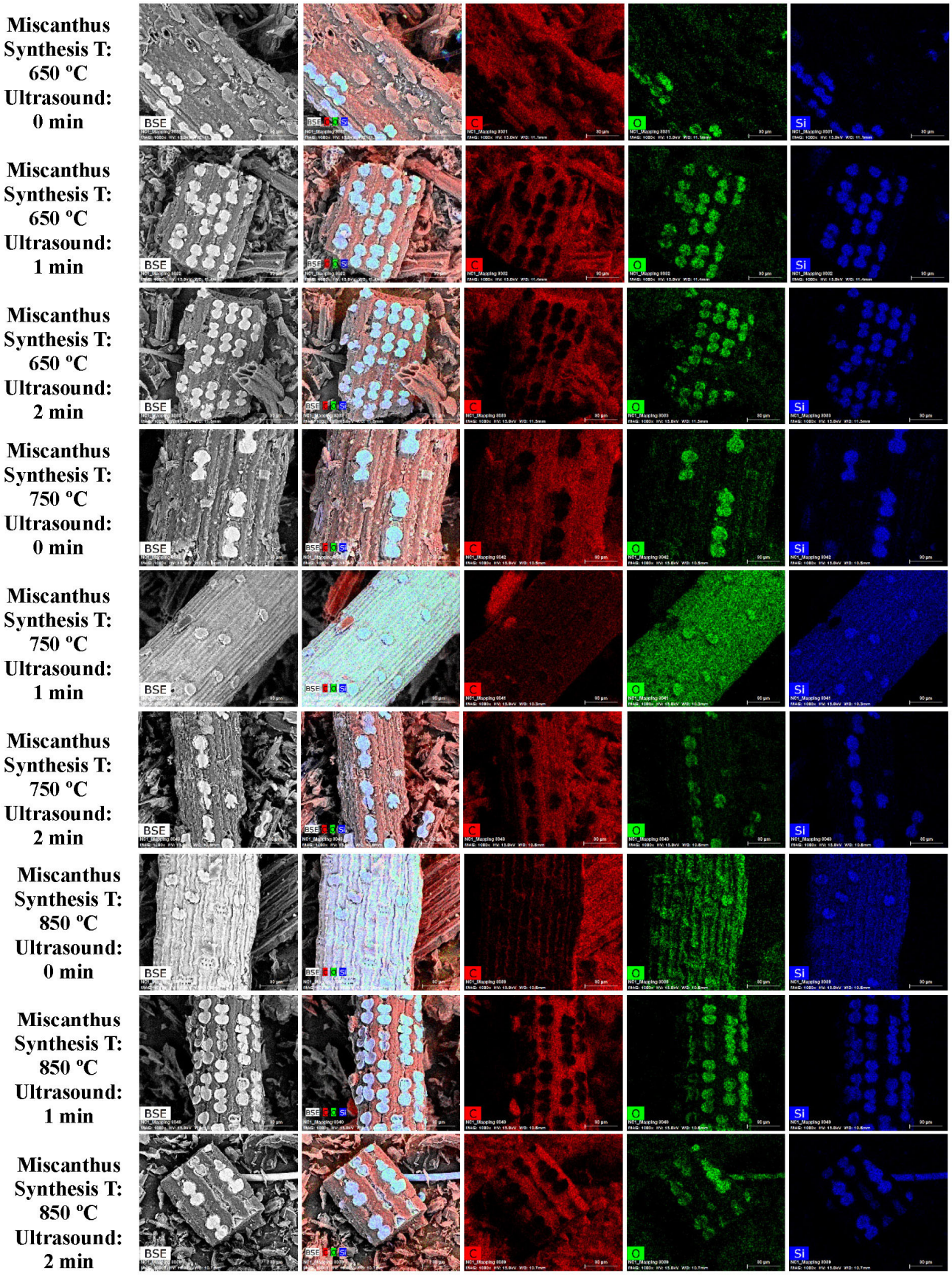


Figure 2. SEM images, BSE images, EDS composite maps, and EDS maps of C, O, and Si elements of biochar samples produced by pyrolysis (at three different temperatures: 650 °C, 750 °C, and 850 °C) of Miscanthus and subjected to ultrasound for different durations (1 & 2 min).

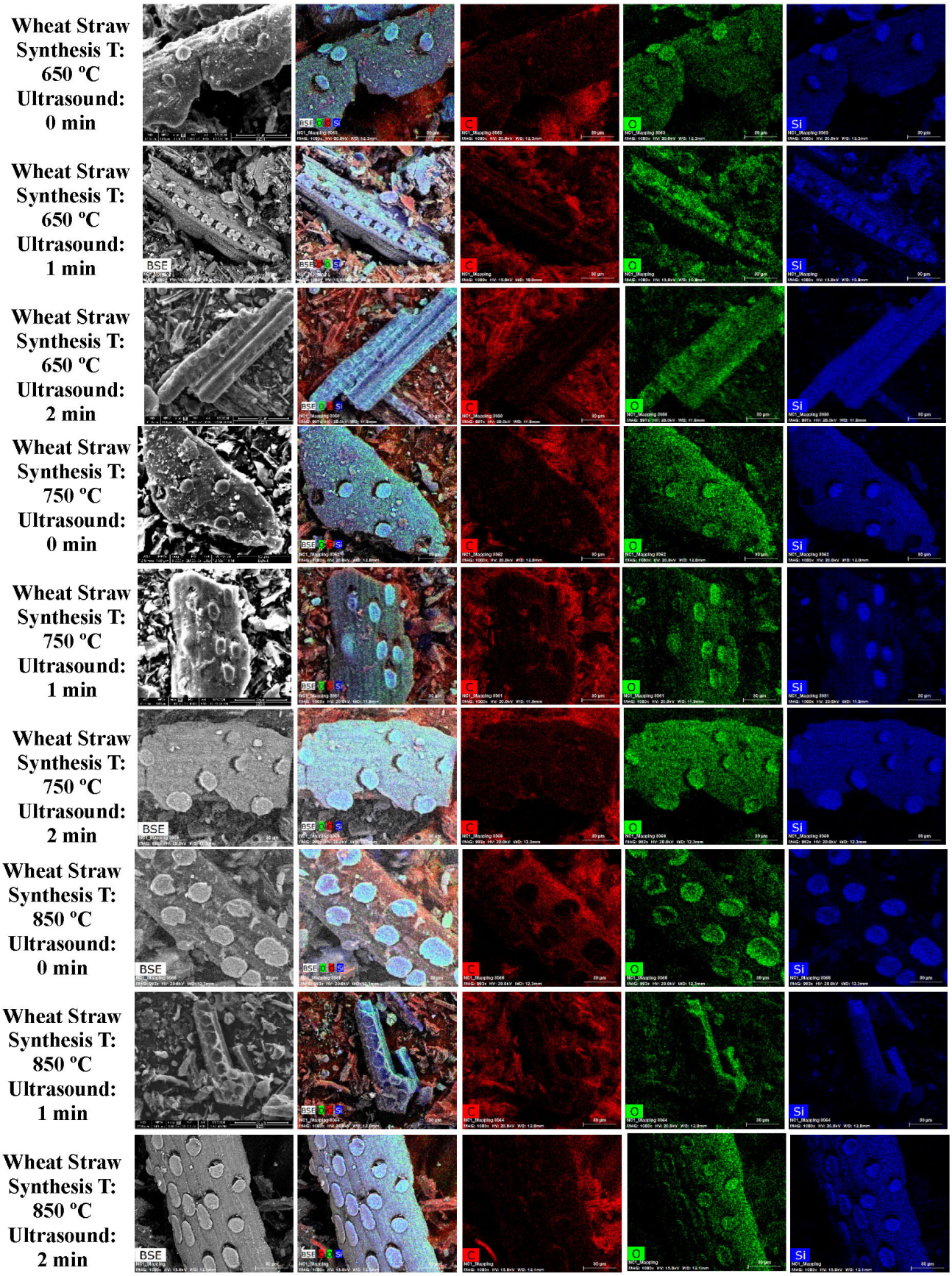


Figure 3. SEM images, BSE images, EDS composite maps, and EDS maps of C, O, and Si elements of biochar samples produced by pyrolysis (at three different temperatures: 650 °C, 750 °C, and 850 °C) of Wheat Straw and subjected to ultrasound for different durations (1 & 2 min).

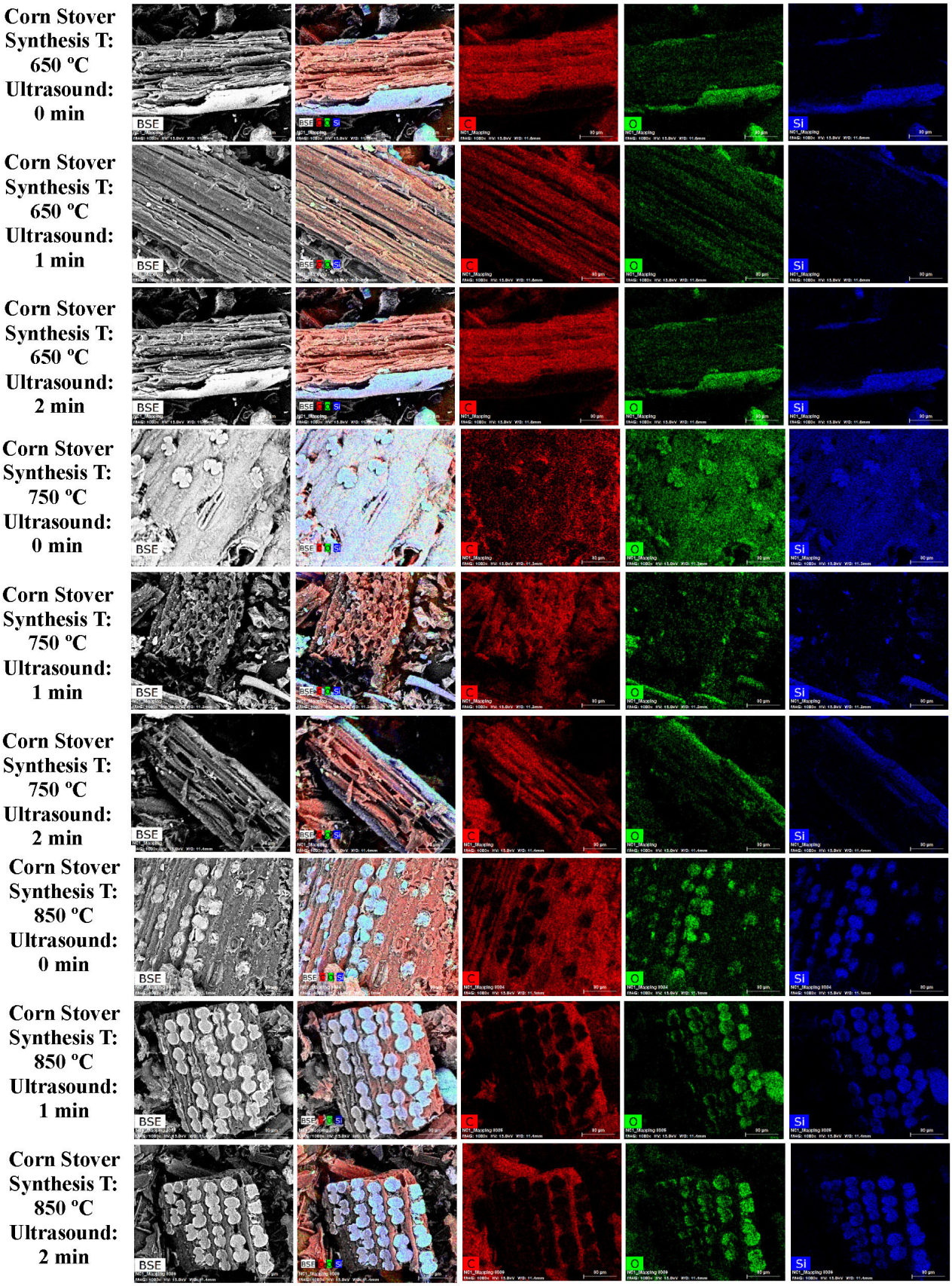


Figure 4. SEM images, BSE images, EDS composite maps, and EDS maps of C, O, and Si elements of biochar samples produced by pyrolysis (at three different temperatures: 650 °C, 750 °C, and 850 °C) of Corn Stover and subjected to ultrasound for different durations (1 & 2 min).

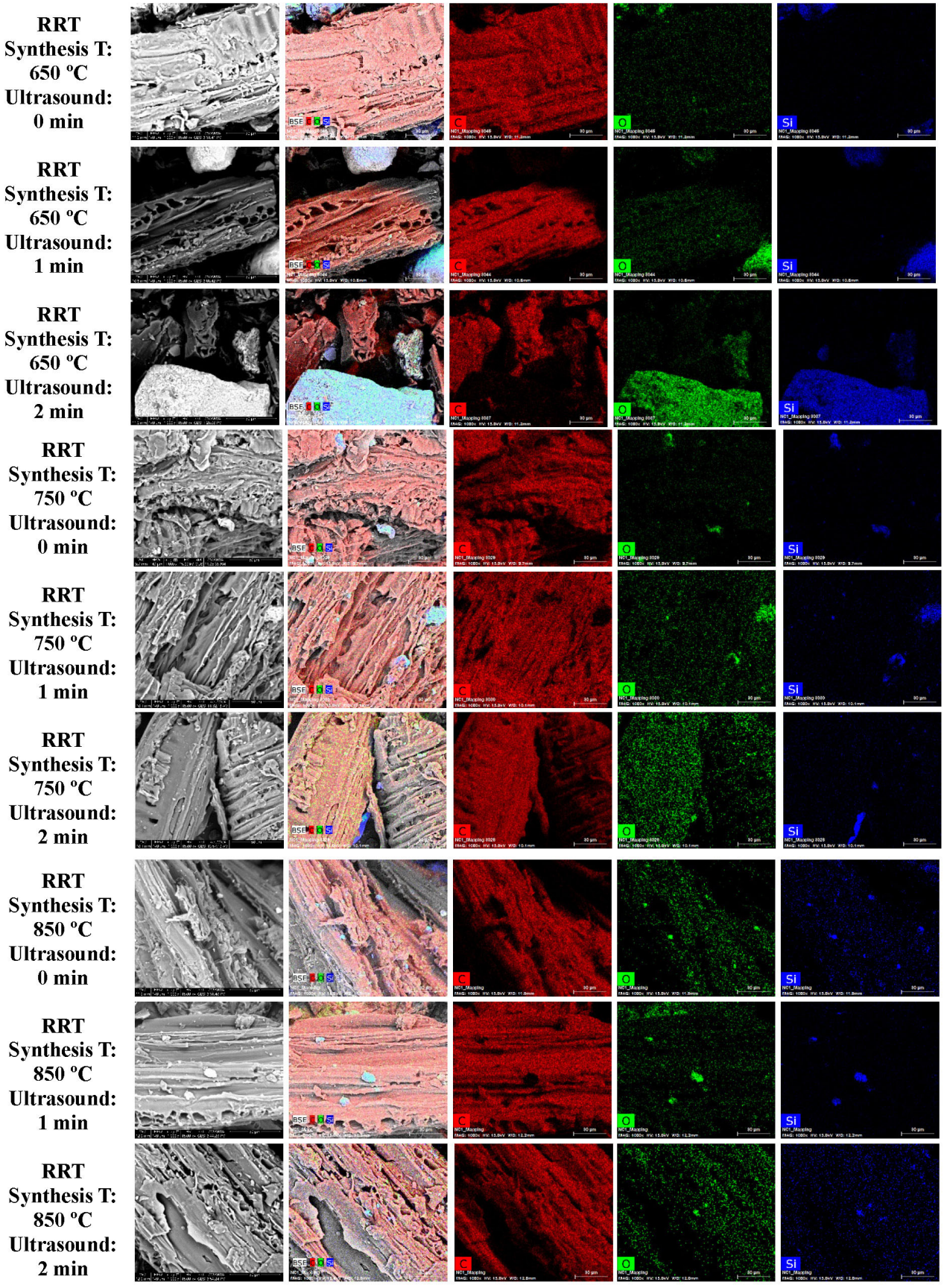


Figure 5. SEM images, BSE images, EDS composite maps, and EDS maps of C, O, and Si elements of biochar samples produced by pyrolysis (at three different temperatures: 650 °C, 750 °C, and 850 °C) of Railroad Ties and subjected to ultrasound for different durations (1 & 2 min).

Ultrasound treatment likely induced cavitation [21], which disrupted the biochar structure and caused the migration of embedded biogenic SiO_2 to the surface. The cavitation events generated during sonication create transient hot spots and microjets exceeding 100 m/s, which impart sufficient localized stress to weaken Si–O–C and Si–C linkages within the biochar–silica interface [22,23]. The resulting increase in surface energy promotes the detachment and redeposition of SiO_2 moieties onto energetically favorable carbon domains, leading to surface enrichment and structural reorganization [23,24]. In addition, when ultrasound waves encounter a solid surface, the differing acoustic impedance between the liquid and the solid causes some of the waves to bounce off the interface while another portion transforms into surface acoustic waves (SAWs), such as surface Rayleigh waves (SRWs). The majority of waves energy becomes focused within the solid, particularly in its immediate vicinity near the surface [25]. SRWs propagate along the interface between the solid and liquid, while also penetrating into the solid structure, generating both vertical and horizontal components of motion in the direction of the waves [26], Figure 6. The penetration depth of SRWs is approximately of the order of the wavelength of the waves [27]. These combined effects contribute to the observed migration and condensation of SiO_2 networks, consistent with previous findings in ultrasonically treated silica–carbon composites. This is mainly true for graphite, where the estimated penetration depth (d) of SRWs is calculated by [28]:

$$\left(\frac{C_{44}}{C_{11}}\right)^{1/2} \ll kd \ll \frac{C_{33}}{C_{11}}\left(\frac{C_{11}}{C_{44}}\right)^{3/2} \quad (1)$$

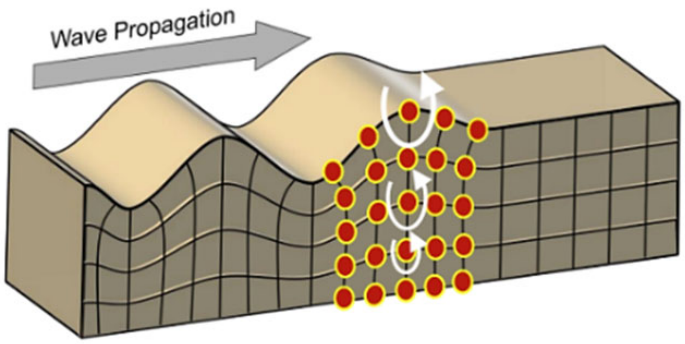


Figure 6. The grey arrow indicates the direction of Rayleigh wave propagation along the surface, while the white arrows represent the instantaneous direction of particle displacement caused by the Rayleigh wave, illustrating the characteristic elliptical motion of particles (indicated by red dot) on and beneath the surface [27,29].

The elastic constants C_{xx} of graphite in various directions determine the wavenumber (k) of the waves, where k is calculated as $k = f.(\rho/C_{44})^{1/2}$, with f representing the ultrasound frequency and ρ denoting the density of graphite [30]. As a result, the penetration depth spans from hundreds of microns to several millimeters, exceeding the biochar's particle (50 to 150 µm) and cluster size (2 to 5 nm) [29].

SEM and EDS analysis reveal that biochar from SG has the highest surface SiO_2 concentration (Figure 1), likely due to its inherently high ash content (10.56%), primarily composed of SiO_2 (79.19%) as shown in Tables 1 and 2. Among all biochars, SG biochar has the most extensive SiO_2 coverage, with maximum coverage in the sample pyrolyzed at 850 °C and exposed to ultrasound for 2 min. Moreover, although SiO_2 is also observed on the surface of the untreated sample, the number of discrete SiO_2 micro-islands increased in samples exposed to ultrasound for 1 and 2 min, particularly at 2 min. Biochar samples produced by the pyrolysis of MIS biomass show relatively lower SiO_2 concentrations

on their surfaces (Figure 2). MIS has a higher volatile matter content (85.53%, Table 1), which reduces ash yield (1.4%, Table 1). However, during pyrolysis, the volatilization of organic components concentrates the SiO_2 in the residual ash, and ultrasound treatment may further enhance this effect by exfoliating the biochar surface and exposing additional SiO_2-rich regions. As observed in Table 2, MIS ash contains a high percentage of SiO_2 (52.31%, Table 2), therefore, migration of silica to the surface is observed due to pyrolysis as well, although ultrasound cavitation can further enhance the SiO_2 migration onto the surface of the biochar in the form of discrete micro islands. Biochar samples produced by the pyrolysis of WS has similar specifications as SG in terms of fixed carbon (13.89%), volatile (77.04%) and ash (9.07%) contents. However, WS has a lower SiO_2 content in its ash compared to SG (58.16% versus 79.19% Table 2). As a result, fewer discrete SiO_2 islands are present on its surface (Figure 3). In addition to these micro-islands, a thin SiO_2 coating is also observed on the biochar's surface (Figure 3). Despite this, biochar produced from WS is likely less susceptible to cavitation as not much difference is observed by exposing to ultrasound waves.

Biochar samples produced by the pyrolysis of CS have a lower ash content (4.3% compared to 10.56% in SG and 9.07% in WS), though 52% of which is composed of SiO_2. The SEM results indicate that synthesis temperature plays a crucial role in the micro-migration of silica. No discrete silica islands are observed on the surface of biochar samples synthesized at 650 °C and 750 °C, even after 2 min of exposure to ultrasound waves (Figure 4). However, in the case of CS biochar synthesized at 850 °C, a strong synergistic interaction with ultrasound waves is observed. This sample showed the highest concentration of SiO_2 and its corresponding elements (Si and O) on its surfaces after exposure to ultrasound for 2 min (Figure 4). The high pyrolysis temperature causes the removal of VOCs, reducing the C, H, and O content, and other labile materials from the biomass, which results in an increased formation and retention of biogenic SiO_2 in the biochar matrix [31–34]. The effect of elevated biomass pyrolysis temperature on the pore structure development of the resulting biochar is substantiated by BET surface area and pore volume data of the biochars derived from the similar biomass feedstocks at different pyrolysis temperature (Section 3.4) [17]. The surface area of the biochar derived by the pyrolysis of MS at 600 °C (303 $m^2\ g^{-1}$) is more than that of the biochar derived by the pyrolysis of MS at 500 °C (119 $m^2\ g^{-1}$) [17]. The corresponding pore volumes also show the significant difference (0.14 → 0.06 $cm^3\ g^{-1}$). These results confirm that elevated pyrolysis temperature facilitates graphitization and pore widening, yielding a more open and thermally stable structure. The consistency of these quantitative trends from the study [17] with the morphological evidence observed in the this study strengthens the interpretation that high biomass pyrolysis temperature enhances the surface area and porosity of the resulting biochar. Moreover, elevated temperatures also foster the formation of stable Si-O-Si bonds within the biochar structure, as identified by the characteristic peaks in the FTIR analysis (Section 3.2), thus increasing both the SiO_2 content and its stability.

The biochar samples produced by the pyrolysis of RRTs showed no discernible presence of SiO_2 and its corresponding elements (Si and O) on their surfaces after ultrasound treatment (Figure 5). This can be explained by the very low or negligible concentration of ash (0.4%) in the RRTs, compared to more naturally siliceous materials like MIS or WS.

RRTs are typically made from wood, which has undergone chemical treatments and possibly preservation processes, and contains SiO_2 in the range of 0.07% to 3% [35,36]. The chemical treatment and preservation processes used in creating RRTs likely reduce or eliminate SiO_2 content in the wood, leaving little to no SiO_2 in the final product (RRTs).

Table 3 is showing the the surface Si atomic % (quantitative EDS analysis of the biochar samples produced from wheat straw pyrolyzed at temperature 850 °C and exposed to

ultrasound for 0, 1, and 2 min. We focused on wheat straw as a representative case to clearly demonstrate the effect of ultrasound on surface Si enrichment. The results confirm that biochars exposed to ultrasound exhibit higher surface Si atomic %, highlighting the migration and surface enrichment phenomenon.

Table 3. Si atomic % on the biochar surface produced by pyrolysis of WS at different temperatures, and exposed to ultrasound for different durations.

Sample	Element	Atomic %
WS-850-0	Silicon	2.47346
WS-850-1	Silicon	22.67204
WS-850-2	Silicon	28.19271

3.2. FTIR Analysis

The FTIR spectra (Figure 7) of biochar samples exhibited several absorption bands associated with Si-containing functional groups, present in biochar. These absorption bands are: at 450 cm^{-1}, representing siloxane (Si–O–Si) functional groups (linkages), with Si–O–Si bonds exhibiting bending vibrations, and/or O–Si–O bonds with bending vibrations [37,38]; at 570 cm^{-1}, indicating siloxane (Si–O–Si) functional groups (linkages), with Si–O–Si bonds exhibiting bending and/or stretching vibrations [37,39]; at 780 cm^{-1}, representing siloxane (Si–O–Si) functional groups (linkages), with Si–O–Si bonds exhibiting symmetric stretching vibrations, and/or Si–C bonds with stretching vibrations [38,40–42]; at 860 cm^{-1}, indicating methylsilane ($Si–CH_3$) functional groups, with Si–C bonds exhibiting stretching vibrations, or Si–O bonds with stretching vibrations, and/or siloxane (Si–O–Si) functional groups (linkages), with Si–O–Si bonds exhibiting stretching vibrations [42,43]; and at 1030 cm^{-1}, representing siloxane (Si–O–Si) functional groups (linkages), with Si–O–Si bonds exhibiting asymmetric stretching vibrations [37,40–46]. By comparing the intensities of all the absorption bands representing Si-containing functional groups, it is evident that the absorption band at 1030 cm^{-1} has the highest intensity (Figure 7). This suggests that siloxane (Si–O–Si) functional groups (linkages), with Si–O–Si bonds exhibiting asymmetric stretching vibrations, are the dominant Si-containing functional groups in biochar.

Siloxane (Si–O–Si) functional groups (linkages) form the backbone of many Si-based materials and contribute significantly to their structural integrity and chemical properties. The presence of siloxane (Si–O–Si) functional groups (linkages) in biochar, as confirmed by the FTIR spectra with absorption bands at 450 cm^{-1} and 1030 cm^{-1} (Figure 7), indicates the existence of SiO_2 compounds and/or SiO_2 networks (a silicate tetrahedron $[SiO_4]^{-4}$ is a structural unit in which central Si atom is bonded to four O atoms, and a SiO_2 network consists of interconnected silicate tetrahedra) in biochar. The intensity of the absorption band at 1030 cm^{-1} is significantly higher compared to that of the absorption band at 450 cm^{-1} (Figure 7), suggesting that siloxane (Si–O–Si) functional groups (linkages), with Si–O–Si bonds exhibiting asymmetric stretching vibrations, dominate in biochar. This observation indicates that the Si–O bonds are inherently strong and that the SiO_2 compounds and/or SiO_2 networks present in biochar are hydrophobic (water-repellent), highly rigid, and resistant to corrosion and other chemical reactions.

The absorption band at 450 cm^{-1} (spanning from around 400 cm^{-1} to 530 cm^{-1}) and the absorption band at 1030 cm^{-1} (ranging from around 900 cm^{-1} to approximately 1280 cm^{-1}) are broader and less intense (Figure 7), indicating that the SiO_2 compounds and/or SiO_2 networks present in biochar are amorphous in nature.

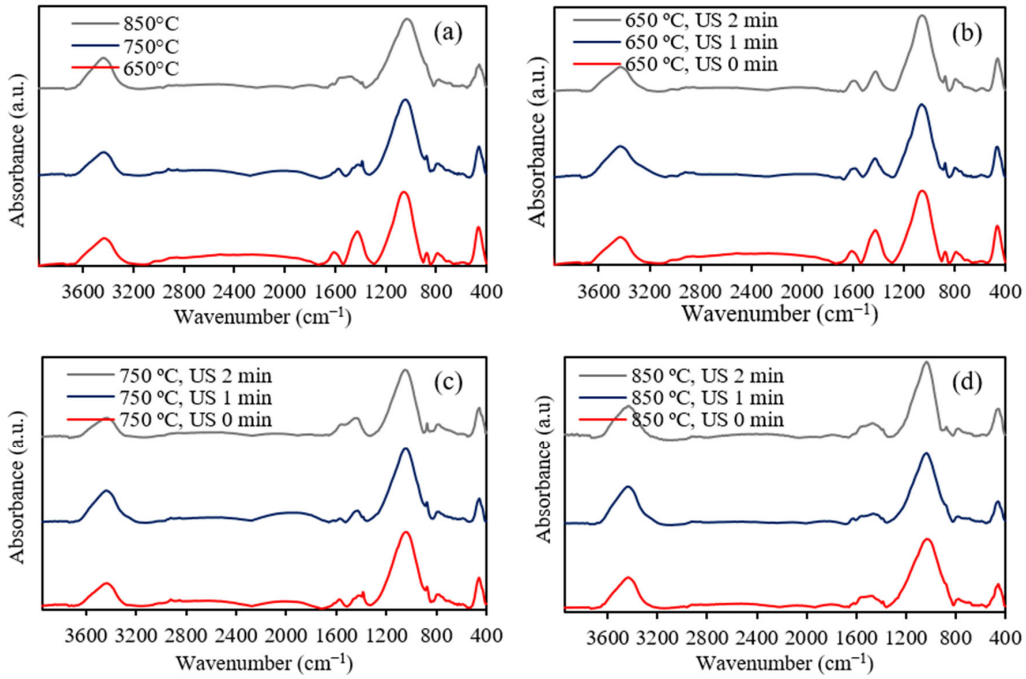


Figure 7. FTIR spectra of biochar (**a**) produced by pyrolysis of biomass (Miscanthus) at different temperatures, (**b**) produced at 650 °C and exposed to ultrasound for different durations, (**c**) produced at 750 °C and exposed to ultrasound for different durations, and (**d**) produced at 850 °C and exposed to ultrasound for different durations.

FTIR spectra (Figure 7) showed several other absorption bands that are not related to Si-containing functional groups but provide valuable insights into the chemistry of the biochar. These absorption bands are at 1400 cm^{-1}, representing C–O bonds with stretching vibrations, or C–C bonds with stretching vibrations, and/or C–H bonds with bending vibrations; at 1600 cm^{-1}, indicating C=C bonds with stretching vibrations; and at 3410 cm^{-1}, representing –OH functional groups, with O–H bonds exhibiting stretching vibrations. The absorption band at 1400 cm^{-1} and the absorption band at 1600 cm^{-1} have relatively low intensity (Figure 7), suggesting that C–O, C–C, and C=C bonds are present in smaller quantities or are less prominent in biochar. On the other hand, the absorption band at 3410 cm^{-1} is quite pronounced (Figure 7), indicating a significant presence of hydroxyl (–OH) groups, which are typically linked to surface hydroxylation, contributing to the biochar's hydrophilicity and potential for water retention.

The changes observed in the FTIR spectra, particularly the increased intensity of the 1030 cm^{-1} band and the attenuation of the 450 cm^{-1} band, indicate enhanced surface condensation of SiO_2 networks accompanied by a relative decrease in bulk silicate features. In transmission (KBr pellet) mode, the infrared signal probes both surface and near-surface layers [47]; however, compositional segregation during ultrasonic activation can result in surface-dominated spectral responses. The strong cavitation and interfacial shear produced during sonication likely promote the exposure and reorganization of Si–O–Si frameworks on the biochar surface [21,48]. Comparable spectral evolution, with intensified Si–O–Si stretching and diminished bending modes, has been reported for ultrasonically modified silica–carbon systems undergoing surface enrichment [48,49]. Although ultrasound-induced removal of C–O groups may slightly influence the 1200–1600 cm^{-1} region, such effects cannot account for the selective increase of the 1030 cm^{-1} Si–O–Si band [48–50]. Hence, the spectral evolution is attributed primarily to the surface migration and condensation of SiO_2 networks rather than to artifact-related alterations To further strengthen the claim that the 1030 cm^{-1} increase arises from surface migration (rather

than only from removal of overlying organics), we therefore use the FTIR results together with SEM/EDS surface maps that directly show increased surface Si and O signals after sonication; the agreement between surface-sensitive FTIR trends and independent surface elemental mapping supports the surface enrichment hypothesis.

Ultrasound-assisted extraction offers significant qualitative advantages over conventional chemical or thermal extraction methods for silica recovery from biochar. Ultrasonic cavitation generates localized microenvironments with high temperatures and pressures, which enhance the release of embedded silica under mild bulk conditions (20–60 °C, short durations of 30 s to few minutes). This contrasts sharply with traditional approaches that require strong mineral acids or prolonged heating above 500 °C, which are energy-intensive and chemically demanding. Ultrasonic methods thus reduce reagent consumption and energy use while minimizing environmental hazards. Additionally, ultrasound can improve surface porosity and functional group accessibility, further facilitating extraction and modification without degrading biochar structural integrity [22,23]. Consequently, ultrasound-assisted extraction achieves comparable or superior efficiency with substantially lower chemical and thermal inputs, making it a more sustainable and economically favorable technique.

3.3. Impact of Ultrasound on Si-Containing Functional Groups in Biochar

The impact of ultrasound on Si-containing functional groups in biochar was examined by comparing the FTIR spectra of biochar samples produced from the same biomass (MIS) via pyrolysis at the same temperature but subjected to ultrasound for different durations. The FTIR spectra of biochar samples (produced at 650 °C and 750 °C) subjected to ultrasound for 1 min and 2 min exhibited notable changes compared to the FTIR spectra of biochar samples not subjected to ultrasound (Figure 7b,c). Firstly, there was a subtle decrease in the intensity (absorbance value) of the absorption band at 450 cm^{-1} (Figure 7b,c). The subtle reduction in the intensity (absorbance value) of the absorption band at 450 cm^{-1} indicates that ultrasound causes the rearrangement of SiO_2 compounds and/or breakdown and rearrangement of the larger SiO_2 networks within the biochar structure. Furthermore, there was a notable increase in the intensity (absorbance value) of the absorption band at 1030 cm^{-1} (Figure 7b,c). FTIR technique primarily interacts with the surface or near-surface regions of the material. The intensity (absorbance value) of the absorption band in the FTIR spectra reflects the concentration of the specific functional groups or substances present in the sample. High intensity (absorbance value) typically suggests that the measured substance (such as a functional group or bond) is present in greater concentration or is more prominent on the surface of the sample. Thus, the increased intensity (absorbance value) of the absorption band at 1030 cm^{-1} suggests that ultrasound induces the breakdown of larger SiO_2 and the migration of SiO_2 compounds and/or SiO_2 networks from within the biochar structure through micropores to the surface. This explanation of the effect of ultrasound on SiO_2 compounds and/or SiO_2 networks in biochar is supported by the SEM and EDS results, as SEM showed more SiO_2 on the surface of ultrasound-treated biochar samples, and EDS exhibited higher concentrations of Si and O elements on the surface of these biochar samples. The increased SiO_2 concentration on the biochar surface may enhance its reactivity and adsorption capacity, thereby making it valuable for various applications.

Additionally, a notable decrease in the intensity (absorbance value) of the absorption band at 1400 cm^{-1} was observed (Figure 7b,c), suggesting that ultrasound might selectively remove or modify surface C–O bonds and/or C–C bonds in biochar. This alteration in surface chemistry may impact the biochar's overall reactivity and its interaction with the environment. The minimal change in the intensity of the absorption band at 1600 cm^{-1} (Figure 7b,c) indicates that the core C structure of the biochar remains largely unaffected by

ultrasound, preserving its overall stability. Ultrasound also led to the broadening of the absorption band at 3410 cm^{-1} (Figure 7b,c). This broadening suggests that ultrasound causes an increase in surface hydroxylation, which may enhance the biochar's hydrophilicity and improve its ability to retain water.

In the FTIR spectra of biochar samples (produced by the pyrolysis at 850 °C) subjected to ultrasound for 1 min and 2 min, several important changes were observed compared to the FTIR spectra of biochar not subjected to ultrasound (Figure 7d). The absorption band at 570 cm^{-1} and the absorption band at 780 cm^{-1} nearly disappeared, while the intensity of the absorption band at 450 cm^{-1}, at 860 cm^{-1}, and at 1030 cm^{-1} increased (Figure 7d). These observed changes suggest that larger SiO_2 networks, Si–O bonds, and/or Si–O–C bonds in biochar produced at higher pyrolysis temperatures (>750 °C) are more susceptible to breakdown by ultrasound. The changes also indicate that SiO_2 compounds and/or SiO_2 networks in biochar produced by pyrolysis at higher temperatures (>750 °C)) can migrate more easily from within the biochar structure through micropores to the surface. This interpretation of the amplified impact of ultrasound on SiO_2 compounds and/or SiO_2 networks in biochar produced by pyrolysis at higher temperatures (>750 °C) is supported by the SEM and EDS results. SEM showed a higher presence of SiO_2 on the surface of ultrasound-treated biochar samples produced by pyrolysis at 850 °C, compared to ultrasound-treated biochar samples produced at 650 °C and 750 °C. Furthermore, EDS analysis showed higher concentrations of Si and O elements on the surface of ultrasound-treated biochar samples produced at 850 °C, compared to ultrasound-treated biochar samples produced at 650 °C and 750 °C. The ultrasound-treated biochar produced by pyrolysis at higher temperatures (>750 °C), with its higher SiO_2 content on the surface, may be a better choice than the ultrasound-treated biochar produced at lower temperatures (<750 °C) for certain applications, particularly those requiring increased reactivity and adsorption capacity.

Interestingly, there was a slight increase in the intensity of the absorption band at 1400 cm^{-1} (Figure 7d). This was in contrast to the decrease in the intensity of the absorption band at 1400 cm^{-1}, observed in the FTIR spectra of ultrasound-treated biochar samples produced at lower temperatures (650 °C and 750 °C) (Figure 7b,c), suggesting that the C–O bonds, C–C bonds, and/or C–H bonds, in biochar produced at higher temperatures (>750 °C), are more resistant to ultrasound-induced breakdown/modifications. The intensity of the absorption band at 1600 cm^{-1} remained stable (Figure 7d), similar to the absorption band at 1600 cm^{-1}, observed in the FTIR spectra of ultrasound-treated biochar samples produced at lower temperatures (650 °C and 750 °C) (Figure 7b,c), confirming that the core C structure of biochar remains intact. The broadening of the absorption band at 3410 cm^{-1} was observed (Figure 7d), similar to the observation in the FTIR spectra of ultrasound-treated biochar samples produced at lower temperatures (650 °C and 750 °C) (Figure 7b,c), indicating that ultrasound enhances surface hydroxylation in biochar, regardless of the pyrolysis temperature applied for its production.

3.4. Applications of Pristine and Engineered Biochar

Exposure of biochar to ultrasound waves can increase porosity and induce silica migration to the surface. The enhancement in porosity and surface area observed upon ultrasonic treatment is supported by quantitative BET measurements reported for similar biochars by the corresponding author [17]. In that study, ultrasonication increased the microporous surface area and total pore volume for various biomass-derived biochars, as summarized in Figure 8 [17]. For instance, the BET surface area increased from 303 to 520 m^2/g for MS-derived biochar, from 290 to 486 m^2/g for SG-derived biochar, and from 284 to 399 m^2/g for CS-derived biochar upon sonication. The pore volumes exhibited a similar trend, reaching

up to 0.21 cm^3/g for MS-derived biochar. These results clearly demonstrate that ultrasound cavitation promotes exfoliation of graphitic layers, removal of occluded mineral matter, and opening of micropores, thereby enhancing the accessible surface area for further modification. The morphology changes observed by SEM in the present study (Figures 1–5) are consistent with this pore development behavior. Increased porosity and induce silica migration to the biochar surface open the opportunities for diverse applications, from removing organic pollutants from water to advancements in the cement industry.

Samples	Microporosity		Micro-mesoporosity	
	Surface area (m^2/g)	Pore volume (cc/g)	Surface area (m^2/g)	Pore volume (cc/g)
R-MS 500	119	0.06	168	0.08
R-MS 600	303	0.14	345	0.18
R-MS 700	324	0.15	368	0.18
R-MS 800	316	0.14	390	0.20
R-SG 500	115	0.06	162	0.08
R-SG 600	290	0.14	325	0.15
R-SG 700	325	0.15	344	0.18
R-SG 800	311	0.14	351	0.18
R-CS 500	96	0.05	149	0.08
R-CS 600	284	0.14	293	0.14
R-CS 700	298	0.14	308	0.14
R-CS 800	288	0.14	357	0.18
R-SB 500	83	0.05	138	0.08
R-SB 600	221	0.11	273	0.14
R-SB 700	236	0.12	289	0.14
R-SB 800	240	0.12	290	0.14
US-MS 500	323	0.15	388	0.20
US-MS 600	520	0.21	581	0.21
US-MS 700	532	0.21	588	0.21
US-MS 800	526	0.21	576	0.21
US-SG 500	309	0.14	374	0.20
US-SG 600	486	0.17	544	0.21
US-SG 700	520	0.21	570	0.21
US-SG 800	503	0.21	550	0.21
US-CS 500	215	0.11	279	0.14
US-CS 600	399	0.20	454	0.20
US-CS 700	423	0.20	473	0.21
US-CS 800	407	0.20	452	0.20
US-SB 500	192	0.11	250	0.13
US-SB 600	332	0.15	382	0.20
US-SB 700	352	0.18	400	0.20
US-SB 800	358	0.18	403	0.20

R, Raw; US Ultrasound Activated; MS, Miscanthus; SG, Switchgrass; CS, Corn Stover; SB, Sugarcane Bagasse

Figure 8. Surface area analysis of raw and sono-chemically activated biochars samples synthesized at different pyrolysis temperatures [17].

Conventional Biochar in Cementitious Matrix: Cement-based materials at low water-to-binder ratios are prone to early-age cracking induced by autogenous shrinkage. External curing with water is a common practice for restricting shrinkage of concrete. However, it may not be efficient for mixtures with low water-to-cement ratio, low porosity and permeability mixtures, because water does not penetrate beyond the surface layers of the concrete [51]. The porous structure of biochar can act as an internal curing agent. Superior water retention properties, yet the hydrophobic nature of biochar allows it to adsorb and restore water during the cement mixing, while releasing water if the neighboring humidity reduces during concrete hardening [51]. Water migration from biochar to concrete increases the effective water to cement ratio after the concrete will set and offsets the empty pore spaces of the matrix created during the chemical shrinkage reactions at the early stages of hydration [52].

Ultrasound-Treated Biochar in Cementitious Matrix: The thin thicknesses of cement paste around aggregates, called the interfacial transition zone [38] is known to have unfavorable properties (larger porosity, lower mechanical strength, higher permeability) [53]. The ITZ is the weakest link in concrete, meaning that microcracks often initiate in this region. Under stress concentration and higher loading, microcracks may develop into macrocracks or become connected to the adjacent microcracks, forming branches and resulting in failure. SiO_2 on the surface of biochar can act as a pozzolanic material. Pozzolanic reactions occur when pozzolanic materials (e.g., silica-rich substances) react with calcium hydroxide [$Ca(OH)_2$] in the presence of water to form additional calcium silicate hydrates (C-S-H), which enhance the strength and durability of cement. This reaction ($SiO_2 + Ca(OH)_2 + H_2O \rightarrow C-S-H$) is crucial in blended cement that incorporate supplementary cementitious materials (SCMs) like fly ash, silica fume, and rice husk ash. C-S-H phase inhibits the formation of micro-cracks between the biochar aggregate and the cement matrix.

Conventional Biochar in Asphalt Matrix: Biochar-modified asphalt, with 5% to 15% biochar content, improves asphalt's complex modulus, penetration, and high-temperature stability. Biochar enhances asphalt's aging resistance and reduces rutting at high temperatures. Additionally, biochar improves asphalt's ability to adsorb VOCs, including alkanes, polycyclic aromatic hydrocarbons (PAHs), and sulfur compounds, which helps reduce harmful emissions. This adsorption capacity is also enhanced at higher temperatures, offering both performance and environmental benefits [54]. However, despite these benefits, they are prone to oxidation aging. Although incorporating silica nanoparticles can improve the aging resistance, their effectiveness is limited by their poor dispersion in the matrix.

Ultrasound-Treated Biochar in Asphalt Matrix: Silica coated biochar may enhance the service life of asphalt particularly in cold regions. This is attributed to stronger hydrogen bonding or dipole-dipole interactions between silica and polar groups in the matrix of asphalt binder increasing fracture energy and rutting resistance.

Conventional Biochar in Wastewater Treatment: Biochar has shown promising results in removing heavy metals such as Zn^{2+}, As^{3+}, and Pb^{2+} by means of physical adsorption, ion exchange, complexation, electrostatic interactions and precipitation occurring either simultaneously or independently which are the main adsorption mechanisms for heavy metals on biochar [55]. However, its efficiency to remove contaminants is limited by factors such as surface area, porosity and pyrolysis conditions.

Ultrasound-Treated Biochar in Wastewater Treatment: It has been continuously proven that organic functional groups (e.g., $-COOH$, $C=O$), inorganic minerals (e.g., carbonates, silicates), and cations (e.g., Na^+, Ca^{2+}, Mg^{2+}) in biochar play a key role in removing the heavy metal ions [56–60]. Certain anions (e.g., CO_3^{2-}, PO_4^{3-}, SiO_4^{4-}) can further enhance heavy metal removal through co-precipitation reactions [61]. A novel and underexplored

modification approach involves synthesizing Si-modified biochar via ultrasound treatment with intentionally elevated silicon concentrations to remediate heavy metals in soils. The silica rich biochar promotes ion exchange between metal cations and silicates, producing metallic silicate precipitation and reducing the mobility of hazardous metals [61–63]. Si containing functional groups provide sufficient adsorption sites to facilitate the complexation of Cd^{2+} and form $CdSiO_3$ precipitate through chemical chelation and ion exchange [64].

Moreover, this biochar can function as a framework for holding fertilizers, while the silica, with its adjustable dissolution properties, can serve as channel for releasing the fertilizers, enabling adaptive, controlled release. Si application in soil has been reported to have a significant effect on decreasing total arsenic concentrations in plant tissue, which is otherwise highly toxic and resistant to removal from the environment [65].

Conventional Biochar in CO_2 Capture: Biochar can be used as an effective CO_2 adsorbent due to its porous structure and presence of basic functional groups. The use of pristine biochar for CO_2 capture is hampered by low porosity and poor surface chemistry. The physisorption of CO_2 onto biochar primarily depends on its pore structure and surface area, whereas chemisorption is largely influenced by the Lewis acid-base interactions associated with the surface functional groups [66]. Therefore, it needs modification via modern techniques to improve its physicochemical properties, such as specific surface area, pore structure, and surface functional groups like nitrogen and sulfur containing groups that increase the basicity and increase the affinity towards CO_2 via dipole-dipole, H bonding and covalent bonding [67–70]. However, an increase in the specific surface area of biochar can only be achieved if activation of biochar is done without damaging its structure.

Ultrasound-Treated Biochar in CO_2 Capture: Physical adsorption is the main mechanism for CO_2 capture. Biochar, with its high surface area, porous structure, and strong hydrophobic and highly aromatized properties, shows great potential as a CO_2 adsorbent, especially when enhanced by ultrasound treatment. The role of biochar's pores in CO_2 capture can be summarized as follows: (1) macropores primarily serve as diffusers, allowing CO_2 to fully contact the biochar material, (2) mesopores act as transporters, facilitating CO_2 movement within their channels, and (3) micropores are the key sites for CO_2 adsorption and storage [71]. Due to its hydrophobic nature, attributed to the abundance of siloxane (O-Si-O) bonds, ultrasound treated biochar exhibits a high CO_2 adsorption capacity, making it an effective carbon sequestration material.

Practical considerations and limitations: While the ultrasound-treatment described herein offers a promising route to mobilise biogenic SiO_2 to the surface of biochar for enhanced reactivity, several practical issues must be borne in mind when scaling toward real-world applications. First, the cost and scalability of applying high-power ultrasound (20 kHz, 700 W in our current study) to large volumes of biochar must be considered: continuous high-power sonication for industrial-scale quantities may entail significant capital and operating expenditures (sonotrode systems, power consumption, cooling, maintenance, etc. [72]). Although specific cost-data for material-processing ultrasound are scarce, studies in related fields note the high energy demand and equipment investment for cavitation-based treatments [72–75]. Second, the long-term stability of the surface-migrated SiO_2 under field or composite conditions remains to be demonstrated: while silica-rich biochars show enhanced oxidation resistance [76,77], the potential for SiO_2 mobilisation, detachment or re-distribution under specific mechanical, chemical or thermal stresses may reduce the functional benefit in service. Third, in soil or composite matrices the potential for SiO_2 loss or migration should be acknowledged: biochar particles incorporated in cementitious or asphalt matrices, or amended in soils, may experience abrasive wear, dissolution, or SiO_2 particle detachment over time and thus a decline of the beneficial

surface-coated SiO_2. Hence, although our results indicate promising enhancements, further work is needed to quantify energy cost per mass of biochar treated, to assess the durability of the SiO_2 layer under application conditions and to evaluate retention of SiO_2 in realistic matrices and environmental contexts.

4. Conclusions

Ultrasound treatment induces the migration of embedded biogenic SiO_2 to the surface of the biochar, as confirmed by SEM and EDS analyses. FTIR results highlight that ultrasound treatment causes the rearrangement of siloxane (Si–O–Si) functional groups, enhancing their exposure on the biochar surface. Additionally, ultrasound treatment selectively modifies other surface functional groups, such as C–O and C–C bonds, and increases surface hydroxylation, which may improve the biochar's hydrophilicity and water retention properties.

Biochar samples produced at pyrolysis temperature of 850 °C exhibited a more pronounced effect of ultrasound on embedded SiO_2 migration to its surface, which suggests that these samples may be particularly advantageous for applications requiring enhanced reactivity and adsorption capacity. The results underline the effectiveness of ultrasound as a novel and sustainable method to enhance the surface characteristics of biochar, especially in relation to its SiO_2 content. This enhanced biochar may have significant potential for diverse applications, including water purification, soil amendment, and C sequestration. In addition, silica, as the carbon-negative filler, can be used in asphalt mix and cementitious composites where pozzolanic activity is required. Moreover, the findings open up new directions for utilizing biochar, transforming it from a waste byproduct of biomass pyrolysis into a functional material with increased surface area, reactivity, and environmental utility.

Future studies should focus on exploring the detailed mechanisms governing silica migration and surface coating during ultrasonication, particularly through in situ spectroscopic and microscopic analyses. Incorporating advanced cross-sectional imaging and time-resolved cavitation diagnostics would provide deeper insights into the spatial distribution and bonding behavior of SiO_2 networks. Additionally, optimizing ultrasound parameters such as frequency, power density, and exposure time could enhance material porosity and surface activation in a more energy-efficient manner. Comparative studies involving different biomass precursors and scaling of the sonochemical process to pilot-scale operations would further expand the practical applicability of this approach for sustainable material synthesis.

Author Contributions: Conceptualization, B.S.; methodology, M.P.H.M., M.A. and S.B.; writing—original draft preparation, M.A. and S.B.; writing—review and editing, B.S.; supervision, B.S.; funding acquisition, B.S. All authors have read and agreed to the published version of the manuscript.

Funding: The authors are grateful to the University of Oklahoma (start-up fund).

Institutional Review Board Statement: Not applicable.

Informed Consent Statement: Not applicable.

Data Availability Statement: The original contributions presented in this study are included in the article material. Further inquiries can be directed to the corresponding author(s). The raw data supporting the conclusions of this article, including the original high-resolution SEM images and EDS elemental (individual and composite) maps, were downscaled for manuscript and publisher file-size requirements. The full-resolution files will be made available by the corresponding author on request.

Conflicts of Interest: The authors declare that they have no known competing financial interest or personal relationships that could have appeared to influence the work reported in this paper.

Abbreviations

The following abbreviations are used in this manuscript:

FAO	Food and Agriculture Organization
SG	Sugarcane Bagasse
MIS	Miscanthus
WS	Wheat Straw
CS	Corn Stover
RRTs	Railroad Ties
VOCs	Volatile Organic Compounds
SEM	Scanning Electron Microscopy
EDS	Energy-Dispersive X-ray Spectroscopy
FTIR	Fourier Transform Infrared Spectroscopy
SAWs	Surface Acoustic Waves
SRWs	Surface Rayleigh Waves
ITZ	Interfacial Transition Zone
PAHs	Polycyclic Aromatic Hydrocarbons

References

1. Raza, M.H.; Abid, M.; Faisal, M.; Yan, T.; Akhtar, S.; Adnan, K.M.M. Environmental and Health Impacts of Crop Residue Burning: Scope of Sustainable Crop Residue Management Practices. *Int. J. Environ. Res. Public Health* **2022**, *19*, 4753. [CrossRef]
2. Huang, T.; Ma, J.; Song, S.; Ling, Z.; Macdonald, R.W.; Gao, H.; Tao, S.; Shen, H.; Zhao, Y.; Liu, X.; et al. Health and environmental consequences of crop residue burning correlated with increasing crop yields midst India's Green Revolution. *NPJ Clim. Atmos. Sci.* **2022**, *5*, 81. [CrossRef]
3. Chen, H.; Wang, F.; Zhang, C.; Shi, Y.; Jin, G.; Yuan, S. Preparation of nano-silica materials: The concept from wheat straw. *J. Non-Cryst. Solids* **2010**, *356*, 2781–2785. [CrossRef]
4. Chen, K.; Ng, K.H.; Cheng, C.K.; Cheng, Y.W.; Chong, C.C.; Vo, D.-V.N.; Witoon, T.; Ismail, M.H. Biomass-derived carbon-based and silica-based materials for catalytic and adsorptive applications- An update since 2010. *Chemosphere* **2022**, *287*, 132222. [CrossRef] [PubMed]
5. Hedayati, A.; Lindgren, R.; Skoglund, N.; Boman, C.; Kienzl, N.; Öhman, M. Ash Transformation during Single-Pellet Combustion of Agricultural Biomass with a Focus on Potassium and Phosphorus. *Energy Fuels* **2021**, *35*, 1449–1464. [CrossRef]
6. Liu, Z.; Deng, P.; Zhang, Z. Application of silica-rich biomass ash solid waste in geopolymer preparation: A review. *Constr. Build. Mater.* **2022**, *356*, 129142. [CrossRef]
7. Morales-Paredes, C.A.; Rodríguez-Linzán, I.; Saquete, M.D.; Luque, R.; Osman, S.M.; Boluda-Botella, N.; Joan Manuel, R.-D. Silica-derived materials from agro-industrial waste biomass: Characterization and comparative studies. *Environ. Res.* **2023**, *231*, 116002. [CrossRef]
8. Vassilev, S.V.; Baxter, D.; Andersen, L.K.; Vassileva, C.G. An overview of the chemical composition of biomass. *Fuel* **2010**, *89*, 913–933. [CrossRef]
9. Wang, G.; Dai, Y.; Yang, H.; Xiong, Q.; Wang, K.; Zhou, J.; Li, Y.; Wang, S. A Review of Recent Advances in Biomass Pyrolysis. *Energy Fuels* **2020**, *34*, 15557–15578. [CrossRef]
10. Yang, Y.; Piao, Y.; Wang, R.; Su, Y.; Liu, N.; Lei, Y. Nonmetal function groups of biochar for pollutants removal: A review. *J. Hazard. Mater. Adv.* **2022**, *8*, 100171. [CrossRef]
11. Wang, Y.; Xiao, X.; Xu, Y.; Chen, B. Environmental Effects of Silicon within Biochar (Sichar) and Carbon–Silicon Coupling Mechanisms: A Critical Review. *Environ. Sci. Technol.* **2019**, *53*, 13570–13582. [CrossRef] [PubMed]
12. Puri, L.; Hu, Y.; Naterer, G. Critical review of the role of ash content and composition in biomass pyrolysis. *Front. Fuels* **2024**, *2*, 1378361. [CrossRef]
13. Esteves, T.C.; Rajamma, R.; Soares, D.; Silva, A.S.; Ferreira, V.M.; Labrincha, J.A. Use of biomass fly ash for mitigation of alkali-silica reaction of cement mortars. *Constr. Build. Mater.* **2012**, *26*, 687–693. [CrossRef]
14. Liang, G.; Li, Y.; Yang, C.; Zi, C.; Zhang, Y.; Hu, X.; Zhao, W. Production of biosilica nanoparticles from biomass power plant fly ash. *Waste Manag.* **2020**, *105*, 8–17. [CrossRef]
15. Xu, S.; Zhou, C.; Fang, H.; Zhu, W.; Shi, J.; Liu, G. Synthesis of ordered mesoporous silica from biomass ash and its application in CO_2 adsorption. *Environ. Res.* **2023**, *231*, 116070. [CrossRef]

16. Wang, K.; Peng, N.; Sun, J.; Lu, G.; Chen, M.; Deng, F.; Dou, R.; Nie, L.; Zhong, Y. Synthesis of silica-composited biochars from alkali-fused fly ash and agricultural wastes for enhanced adsorption of methylene blue. *Sci. Total Environ.* **2020**, *729*, 139055. [CrossRef]
17. Chatterjee, R.; Sajjadi, B.; Chen, W.-Y.; Mattern, D.L.; Hammer, N.; Raman, V.; Dorris, A. Effect of Pyrolysis Temperature on PhysicoChemical Properties and Acoustic-Based Amination of Biochar for Efficient CO_2 Adsorption. *Front. Energy Res.* **2020**, *8*, 8. [CrossRef]
18. Asadi, A.; Pourfattah, F.; Miklós Szilágyi, I.; Afrand, M.; Żyła, G.; Seon Ahn, H.; Wongwises, S.; Minh Nguyen, H.; Arabkoohsar, A.; Mahian, O. Effect of sonication characteristics on stability, thermophysical properties, and heat transfer of nanofluids: A comprehensive review. *Ultrason. Sonochem.* **2019**, *58*, 104701. [CrossRef]
19. Pradhan, S.; Hedberg, J.; Blomberg, E.; Wold, S.; Odnevall Wallinder, I. Effect of sonication on particle dispersion, administered dose and metal release of non-functionalized, non-inert metal nanoparticles. *J. Nanopart. Res.* **2016**, *18*, 285. [CrossRef]
20. Hughes, L.; Machado, P.; Johnson, E. Elemental Maps to Dye for: Energy Dispersive X-ray Spectrometry Facilitates a Better Understanding of the Contrast Mechanisms in Common Electron Microscopy Stains. *Microsc. Microanal.* **2023**, *29* (Suppl. S1), 1185–1186. [CrossRef]
21. Wang, J.; Li, W.; Zhao, Z.; Musoke, F.S.N.; Wu, X. Ultrasonic Activated Biochar and Its Removal of Harmful Substances in Environment. *Microorganisms* **2022**, *10*, 1593. [CrossRef] [PubMed]
22. Hoo, D.Y.; Low, Z.L.; Low, D.Y.S.; Tang, S.Y.; Manickam, S.; Tan, K.W.; Ban, Z.H. Ultrasonic cavitation: An effective cleaner and greener intensification technology in the extraction and surface modification of nanocellulose. *Ultrason. Sonochem.* **2022**, *90*, 106176. [CrossRef] [PubMed]
23. Savkina, R.K.; Gudymenko, A.I.; Kladko, V.P.; Korchovyi, A.A.; Nikolenko, A.S.; Smirnov, A.B.; Stara, T.R.; Strelchuk, V.V. Silicon Substrate Strained and Structured via Cavitation Effect for Photovoltaic and Biomedical Application. *Nanoscale Res. Lett.* **2016**, *11*, 183. [CrossRef] [PubMed]
24. Albanese, L.; Baronti, S.; Liguori, F.; Meneguzzo, F.; Barbaro, P.; Vaccari, F.P. Hydrodynamic cavitation as an energy efficient process to increase biochar surface area and porosity: A case study. *J. Clean. Prod.* **2019**, *210*, 159–169. [CrossRef]
25. Ananda, A.A. Propagation of Rayleigh Waves in Thin-Films. Ph.D. Thesis, Department of Physics at W&M University (William & Mary), Williamsburg, VA, USA, 1997.
26. Lewis, M.F. On Rayleigh Waves and Related Propagating Acoustic Waves. In *Rayleigh-Wave Theory and Application*; Ash, E.A., Paige, E.G.S., Eds.; Springer: Berlin/Heidelberg, Germany, 1985; pp. 37–58.
27. Li, Z.; Young, R.J.; Backes, C.; Zhao, W.; Zhang, X.; Zhukov, A.A.; Tillotson, E.; Conlan, A.P.; Ding, F.; Haigh, S.J. Mechanisms of Liquid-Phase Exfoliation for the Production of Graphene. *ACS Nano* **2020**, *14*, 10976–10985. [CrossRef]
28. Kosevich, Y.A.; Syrkin, E.S.; Kossevich, A.M. Vibrations localized near surfaces and interfaces in nontraditional crystals. *Prog. Surf. Sci.* **1997**, *55*, 59–111. [CrossRef]
29. Hess, P. Surface Acoustic Waves in Materials Science. *Phys. Today* **2002**, *55*, 42–47. [CrossRef]
30. Blakslee, O.L.; Proctor, D.G.; Seldin, E.J.; Spence, G.B.; Weng, T. Elastic constants of compression-annealed pyrolytic graphite. *J. Appl. Phys.* **1970**, *41*, 3373–3382. [CrossRef]
31. Bhatia, D.; Saroha, A.K. Effect of Pyrolysis Temperature on Chemical Composition of Biochar Obtained from Pyrolysis of Rice Straw. *Chem. Eng. Process Tech.* **2022**, *7*, 1062.
32. Li, Z.; Su, Q.; Xiang, L.; Yuan, Y.; Tu, S. Effect of Pyrolysis Temperature on the Sorption of Cd(II) and Se(IV) by Rice Husk Biochar. *Plants* **2022**, *11*, 3234. [CrossRef]
33. Zhao, B.; O'Connor, D.; Zhang, J.; Peng, T.; Shen, Z.; Tsang, D.C.W.; Hou, D. Effect of pyrolysis temperature, heating rate, and residence time on rapeseed stem derived biochar. *J. Clean. Prod.* **2018**, *174*, 977–987. [CrossRef]
34. Jindo, K.; Mizumoto, H.; Sawada, Y.; Sanchez-Monedero, M.A.; Sonoki, T. Physical and chemical characterization of biochars derived from different agricultural residues. *Biogeosciences* **2014**, *11*, 6613–6621. [CrossRef]
35. Santana, M.A.E.; Rodrigues, L.C.; Coradin, V.T.R.; Okino, E.Y.A.; Souza, M.R.d. Silica content of 36 Brazilian tropical wood species. *Holzforschung* **2013**, *67*, 19–24. [CrossRef]
36. Kjaer, E.D.; Kajornsrichon, S.; Lauridsen, E.B. Heartwood, Calcium and Silica Content in Five Provenances of Teak (*Tectona grandis* L.) 1. *Silvae Genet.* **1999**, *48*, 1–3.
37. Marchewka, J.; Jeleń, P.; Rutkowska, I.; Bezkosty, P.; Sitarz, M. Chemical Structure and Microstructure Characterization of Ladder-Like Silsesquioxanes Derived Porous Silicon Oxycarbide Materials. *Materials* **2021**, *14*, 1340. [CrossRef]
38. Ritz, M. Infrared and Raman Spectroscopy of Mullite Ceramics Synthesized from Fly Ash and Kaolin. *Minerals* **2023**, *13*, 864. [CrossRef]
39. Mysen, B. Solution mechanisms of COHN fluids in melts to upper mantle temperature, pressure, and redox conditions. *Am. Mineral.* **2018**, *103*, 1780–1788. [CrossRef]
40. Ellerbrock, R.H.; Stein, M.; Schaller, J. Comparing silicon mineral species of different crystallinity using Fourier transform infrared spectroscopy. *Front. Environ. Chem.* **2024**, *5*, 1462678. [CrossRef]

41. Kleinová, A.; Huran, J.; Sasinková, V.; Perný, M.; Šály, V.; Packa, J. FTIR spectroscopy of silicon carbide thin films prepared by PECVD technology for solar cell application. In Proceedings of the Reliability of Photovoltaic Cells, Modules, Components, and Systems VIII, San Diego, CA, USA, 23 September 2015; SPIE: Bellingham, WA, USA, 2015; Volume 9563.
42. Launer, P.; Arkles, B. Infrared Analysis of Organosilicon Compounds. In *Silicon Compounds: Silanes & Silicones*; Gelest Inc.: Morrisville, PA, USA, 2013; pp. 175–178.
43. Jeleń, P.; Bik, M.; Nocuń, M.; Gawęda, M.; Długoń, E.; Sitarz, M. Free carbon phase in SiOC glasses derived from ladder-like silsesquioxanes. *J. Mol. Struct.* **2016**, *1126*, 172–176. [CrossRef]
44. Handke, M.; Handke, B.; Kowalewska, A.; Jastrzębski, W. New polysilsesquioxane materials of ladder-like structure. *J. Mol. Struct.* **2009**, *924–926*, 254–263. [CrossRef]
45. Shahrokh Abadi, M.H. Effects of Annealing Temperature on Infrared Spectra of SiO2 Extracted from Rice Husk. *J. Ceram. Sci. Technol.* **2014**, *5*, 1–5.
46. Oufakir, A.; Khouchaf, L.; Elaatmani, M.; Louarn, G.; Fraj, A. Study of structural short order and surface changes of SiO_2 compounds. *MATEC Web Conf.* **2018**, *149*, 01041. [CrossRef]
47. Hongzhen, T.; Wang, A.; Chen, J.; Jiang, X.-Z.; Shi, J.; Zhang, C.; Mei, Y.; Wang, B. Treatment Effect Modeling for FTIR Signals Subject to Multiple Sources of Uncertainties. *IEEE Trans. Autom. Sci. Eng.* **2021**, *19*, 895–906. [CrossRef]
48. Chaubey, A.K.; Pratap, T.; Preetiva, B.; Patel, M.; Singsit, J.S.; Pittman, C.U., Jr.; Mohan, D. Definitive Review of Nanobiochar. *ACS Omega* **2024**, *9*, 12331–12379. [CrossRef] [PubMed]
49. Wang, Y.; Xiao, X.; Chen, B. Biochar Impacts on Soil Silicon Dissolution Kinetics and their Interaction Mechanisms. *Sci. Rep.* **2018**, *8*, 8040. [CrossRef] [PubMed]
50. Liu, J.; Liu, H.; Yang, X.; Jia, X.; Cai, M.; Bao, Y. Preparation of Si–Mn/biochar composite and discussions about characterizations, advances in application and adsorption mechanisms. *Chemosphere* **2021**, *281*, 130946. [CrossRef]
51. Lura, P.; Wyrzykowski, M.; Tang, C.; Lehmann, E. Internal curing with lightweight aggregate produced from biomass-derived waste. *Cem. Concr. Res.* **2014**, *59*, 24–33. [CrossRef]
52. Dixit, A.; Gupta, S.; Pang, S.D.; Kua, H.W. Waste Valorisation using biochar for cement replacement and internal curing in ultra-high performance concrete. *J. Clean. Prod.* **2019**, *238*, 117876. [CrossRef]
53. Lin, J.; Chen, H.; Zhang, R.; Liu, L. Characterization of the wall effect of concrete via random packing of polydispersed superball-shaped aggregates. *Mater. Charact.* **2019**, *154*, 335–343. [CrossRef]
54. Ma, F.; Dai, J.; Fu, Z.; Li, C.; Wen, Y.; Jia, M.; Wang, Y.; Shi, K. Biochar for asphalt modification: A case of high-temperature properties improvement. *Sci. Total Environ.* **2022**, *804*, 150194. [CrossRef]
55. Kang, X.; Sun, M.; Geng, N.; Li, Y.; Wang, H.; Pan, H.; Yang, Q.; Yang, Z.; Lou, Y.; Zhuge, Y. A novel and recyclable silica gel-modified biochar to remove cadmium from wastewater: Model application and mechanism exploration. *Ecotoxicol. Environ. Saf.* **2024**, *281*, 116608. [CrossRef]
56. Tripathi, A.; Ekanayake, A.; Tyagi, V.K.; Vithanage, M.; Singh, R.; Rao, Y.R.S. Emerging contaminants in polluted waters: Harnessing Biochar's potential for effective treatment. *J. Environ. Manag.* **2025**, *373*, 123778. [CrossRef]
57. Singh, J.; Bhattu, M.; Liew, R.K.; Verma, M.; Brar, S.K.; Bechelany, M.; Jadeja, R. Transforming rice straw waste into biochar for advanced water treatment and soil amendment applications. *Environ. Technol. Innov.* **2025**, *37*, 103932. [CrossRef]
58. Bui, V.K.H.; Nguyen, T.P.; Tran, T.C.P.; Nguyen, T.T.N.; Duong, T.N.; Nguyen, V.T.; Liu, C.; Nguyen, D.D.; Nguyen, X.C. Biochar-based fixed filter columns for water treatment: A comprehensive review. *Sci. Total Environ.* **2024**, *954*, 176199. [CrossRef] [PubMed]
59. Kamali, M.; Appels, L.; Kwon, E.E.; Aminabhavi, T.M.; Dewil, R. Biochar in water and wastewater treatment—A sustainability assessment. *Chem. Eng. J.* **2021**, *420*, 129946. [CrossRef]
60. Gopinath, A.; Divyapriya, G.; Srivastava, V.; Laiju, A.R.; Nidheesh, P.V.; Kumar, M.S. Conversion of sewage sludge into biochar: A potential resource in water and wastewater treatment. *Environ. Res.* **2021**, *194*, 110656. [CrossRef] [PubMed]
61. Liu, L.; Yang, X.; Ahmad, S.; Li, X.; Ri, C.; Tang, J.; Ellam, R.M.; Song, Z. Silicon (Si) modification of biochars from different Si-bearing precursors improves cadmium remediation. *Chem. Eng. J.* **2023**, *457*, 141194. [CrossRef]
62. Li, J.; Zheng, L.; Wang, S.-L.; Wu, Z.; Wu, W.; Niazi, N.K.; Shaheen, S.M.; Rinklebe, J.; Bolan, N.; Ok, Y.S.; et al. Sorption mechanisms of lead on silicon-rich biochar in aqueous solution: Spectroscopic investigation. *Sci. Total Environ.* **2019**, *672*, 572–582. [CrossRef]
63. Li, A.; Lu, T.; Zhang, Y.; Deng, S.; Duan, X.; Qiu, G. Mechanisms for synergistically enhancing cadmium remediation performance of biochar: Silicon activation and functional group effects. *Bioresour. Technol.* **2024**, *404*, 130913. [CrossRef]
64. Cai, T.; Liu, X.; Zhang, J.; Tie, B.; Lei, M.; Wei, X.; Peng, O.; Du, H. Silicate-modified oiltea camellia shell-derived biochar: A novel and cost-effective sorbent for cadmium removal. *J. Clean. Prod.* **2021**, *281*, 125390. [CrossRef]
65. Zama, E.F.; Reid, B.J.; Sun, G.-X.; Yuan, H.-Y.; Li, X.-M.; Zhu, Y.-G. Silicon (Si) biochar for the mitigation of arsenic (As) bioaccumulation in spinach (*Spinacia oleracean*) and improvement in the plant growth. *J. Clean. Prod.* **2018**, *189*, 386–395. [CrossRef]

66. Serafin, J.; Narkiewicz, U.; Morawski, A.W.; Wróbel, R.J.; Michalkiewicz, B. Highly microporous activated carbons from biomass for CO_2 capture and effective micropores at different conditions. *J. CO2 Util.* **2017**, *18*, 73–79. [CrossRef]
67. Guo, S.; Li, Y.; Wang, Y.; Wang, L.; Sun, Y.; Liu, L. Recent advances in biochar-based adsorbents for CO_2 capture. *Carbon Capture Sci. Technol.* **2022**, *4*, 100059. [CrossRef]
68. Baig, S.; Sajjadi, B. Non-thermal plasma enhanced catalytic conversion of methane into value added chemicals and fuels. *J. Energy Chem.* **2024**, *97*, 265–301. [CrossRef]
69. Mohammed, Z.; Jeelani, S.; Rangari, V. Low temperature plasma treatment of rice husk derived hybrid silica/carbon biochar using different gas sources. *Mater. Lett.* **2021**, *292*, 129678. [CrossRef]
70. Abdullah, M.; Sajjadi, B. Sustainable conversion of natural gas to hydrogen using transition metal carbides. *Int. J. Hydrogen Energy* **2024**, *90*, 61–103. [CrossRef]
71. Zhang, C.; Ji, Y.; Li, C.; Zhang, Y.; Sun, S.; Xu, Y.; Jiang, L.; Wu, C. The Application of Biochar for CO_2 Capture: Influence of Biochar Preparation and CO_2 Capture Reactors. *Ind. Eng. Chem. Res.* **2023**, *62*, 17168–17181. [CrossRef]
72. Yao, Y.; Pan, Y.; Liu, S. Power ultrasound and its applications: A state-of-the-art review. *Ultrason. Sonochem.* **2020**, *62*, 104722. [CrossRef]
73. Vouters, M.; Rumeau, P.; Tierce, P.; Costes, S. Ultrasounds: An industrial solution to optimise costs, environmental requests and quality for textile finishing. *Ultrason. Sonochem.* **2004**, *11*, 33–38. [CrossRef]
74. Chatterjee, R.; Sajjadi, B.; Mattern, D.L.; Chen, W.-Y.; Zubatiuk, T.; Leszczynska, D.; Leszczynski, J.; Egiebor, N.O.; Hammer, N. Ultrasound cavitation intensified amine functionalization: A feasible strategy for enhancing CO_2 capture capacity of biochar. *Fuel* **2018**, *225*, 287–298. [CrossRef]
75. Chatterjee, R.; Sajjadi, B.; Chen, W.-Y.; Mattern, D.L.; Hammer, N.; Raman, V.; Dorris, A. Impact of Biomass Sources on Acoustic-Based Chemical Functionalization of Biochars for Improved CO_2 Adsorption. *Energy Fuels* **2020**, *34*, 8608–8627. [CrossRef]
76. Nguyen, M.N. Potential use of silica-rich biochar for the formulation of adaptively controlled release fertilizers: A mini review. *J. Clean. Prod.* **2021**, *307*, 127188. [CrossRef]
77. Li, Z.; Yuan, Y.; Xiang, L.; Su, Q.; Liu, Z.; Wu, W.; Huang, Y.; Tu, S. Silicon-Rich Biochar Detoxify Multiple Heavy Metals in Wheat by Regulating Oxidative Stress and Subcellular Distribution of Heavy Metal. *Sustainability* **2022**, *14*, 16417. [CrossRef]

Disclaimer/Publisher's Note: The statements, opinions and data contained in all publications are solely those of the individual author(s) and contributor(s) and not of MDPI and/or the editor(s). MDPI and/or the editor(s) disclaim responsibility for any injury to people or property resulting from any ideas, methods, instructions or products referred to in the content.